Final Technical Report for
U.S. Geological Survey
National Earthquake Hazard Reduction Program
Award No. 08HQGR0010

Laboratory Investigation of Damage by Tensile Fracture during Dynamic Shear Rupture Propagation

David D. Pollard, P.I.
W. Ashley Griffith

Department of Geological and Environmental Science
Braun Hall, Building 320, Rm. 118
Stanford University
Stanford, CA 94305-2115

Phone: 650-723-4679
Fax: 650-725-0979
Email: dpollard@stanford.edu

Term of Award: Dec 1, 2008-Nov 30, 2009
No-cost Extension though June 30, 2009
Final Report Submitted: July 13, 2009

ABSTRACT

We use optical experiments and high-speed photography to interpret the origins of tensile fractures that form during dynamic shear rupture in laboratory experiments. Sub-Rayleigh (slower than the Rayleigh wave speed, c_R) shear ruptures in Homalite-100 produce damage zones consisting of an array of tensile cracks. These cracks nucleate and grow within cohesive zones behind the tips of shear ruptures that propagate dynamically along interfaces with frictional and cohesive strength, simulating a "strong" fault. The tensile cracks are produced only along one side of the interface where transient, fault-parallel, tensile stress perturbations are associated with the growing shear rupture tip. The experimental results related to this study will be published in Geology in September 2009. In a subsequent manuscript, in preparation, we examine the local dynamic stress field in the vicinity of the tip of the main shear rupture, which is growing along a weak interface with sub-Rayleigh speed. It is this stress field which is responsible for driving the off-fault mode-I microcracks of interest. We show not only that the orientation of the cracks can be explained by this analytical model, but the cracks can be used to constrain the constitutive behavior of the shear rupture tip. In addition, we propose an extension of this model to explain structures observed along exhumed faults. Results of this study represent an important bridge between geological observations of structures preserved along exhumed faults and theoretical models of earthquake propagation, potentially leading to diagnostic criteria for interpreting velocity, directivity, and static pre-stress state associated with past earthquakes on exhumed faults.

INTRODUCTION

Direct observation of ancient faults exhumed from hypocentral depths can provide high-precision data related to the local boundary conditions controlling earthquake rupture propagation (Chester et al., 1993; Wibberley and Shimamoto, 2003; Di Toro et al., 2005a,b; Griffith et al., 2008). However, field-based studies of faults typically address fault development as a quasi-static problem occurring on the time scale of 10^3 to 10^6 years and greater (Willemse and Pollard, 1998; Mutlu and Pollard, 2008). Direct evidence of processes operating on shorter time scales during faulting are generally erased from rocks due to overprinting events, chemical changes, and structural alterations. Differentiating faults that hosted earthquakes from those that slipped aseismically is nearly impossible, save for the rare occurrence of pseudotachylyte, a rock formed by melting associated with frictional heating during earthquakes (Cowan, 1999). Other structural features in rocks that may be indicative of dynamic (earthquake) processes are indistinguishable from quasi-static (aseismic) features because similar structures may hypothetically be formed by non-unique combinations of different variables (i.e., stress, deformation rate, temperature, etc.).

In a series of laboratory studies that provided the first experimental evidence of supershear (greater than the shear wave velocity, c_s) crack growth in an isotropic and homogeneous solid (Homalite-100), Rosakis et al. (2000) observed and analyzed an array of secondary tensile microcracks that formed adjacent to the rupture interface. These microcracks formed dynamically only on one side of the rupture interface (Rosakis et al., 2000). Their occurrence was attributed to dynamic frictional contact and sliding behind the supershear rupture tip (Rosakis et al., 2000, Samudrala et al., 2002). The possible relation of these cracks to

geological observations of periodic arrays of tensile, off-fault, fractures and to pseudotachylyte injection veins was hypothesized by Rosakis (2002).

Di Toro et al. (2005a) provided field evidence that tensile fractures containing pseudoatachylyte (pseudotachylyte injection veins) might indeed form by a similar dynamic process. Pseudotachylyte injection veins along exhumed strike-slip faults in the Adamello batholith in the Italian Alps are observed in quasi-periodic arrays dominantly on one side of and nearly orthogonal to the faults. Such high-angle veins also are common along other pseudotachylyte bearing faults (e.g., Swanson, 1988;) and differ from wing cracks commonly observed near tips of shear discontinuities (faults, sheared joints, and slipped bedding surfaces) related to the quasi-static perturbed stress field introduced by the shearing (Willemse and Pollard, 1998; Mutlu and Pollard, 2008).

If pseudotachylyte injection veins are a dynamic phenomenon related to earthquake propagation, the geometry of tensile crack arrays should provide information about rupture dynamics from exhumed faults. To test this hypothesis we designed an experiment capable of providing values of relevant variables during dynamic tensile microcrack nucleation accompanying high-speed shear rupture.

LABORATORY EXPERIMENTS

The experimental conditions under which tensile microcrack arrays were initially produced (Rosakis et al., 2000, Samudrala et al., 2002) utilized an impact-loading device to nucleate unilateral supershear ruptures. These experiments did not simulate earthquake rupture conditions expected along faults in that the interface was entirely free of compressive pre-stress. In addition, the nature of the impact loading introduces complex transients to the experiments making correlations among crack angle, rupture velocity, and far-field static prestress conditions difficult. In a second set of experiments, sub-Rayleigh and supershear bilateral ruptures were induced in samples subjected to static uniaxial pre-compression (Xia et al., 2004,2005; Lykotrafitis et al., 2006; Lu et al., 2007). In these experiments dynamic ruptures propagated along a frictional (but cohesionless) interface and were induced by an exploding wire embedded within the Homalite; however tensile microcracks, like those observed along natural faults (Swanson, 1988; Di Toro et al., 2005a) and those predicted by numerical experiments (Yamashita, 2000; Di Toro et al., 2005a), were not produced in these experiments, because transient stress concentrations associated with the propagating shear rupture tip did not exceed the materal tensile strength

Here we report for the first time the generation of tensile microcracks that formed dynamically behind a sub-Rayleigh shear rupture propagating along a preexisting interface with cohesive *and* frictional strength, subjected to compressive and shear pre-stress (Fig. 1). Transient stress fields during the experiments are recorded using photoelasticity (Kavaturu et al., 1998) and high-speed digital photography (e.g., Rosakis, 2002), yielding patterns of isochromatic fringes (Fig. 2) that are contours of maximum in-plane shear stress. The asymmetric fringe pattern about the propagating rupture tip (Fig. 2A, B) is a result of a superposition of the static ambient stress, or prestress state (Poliakov et al., 2002; Samudrala et al., 2002) and the transient field around the propagating rupture. The stress state, σ_{ij}, in the vicinity of the propagating shear rupture tip can be written as:

$$\sigma_{ij} = \sigma_{ij}^0 + \Delta\sigma_{ij}, \quad (1)$$

where σ_{ij}^0 is the static ambient stress state due to the remote load *P*, and $\Delta\sigma_{ij}$ is the stress perturbation due to the rupture (Poliakov et al., 2002).

Samudrala et al. (2002) and Poliakov et al. (2002) show that the off-fault stress concentration due to a propagating shear rupture is related to rupture velocity v_{II} and to peak shear traction τ_p attained along the rupture surface (i.e., shear stress needed to overcome total interface strength). In previous laboratory studies, this total interface strength τ_p was either due to cohesive strength, τ_o, of the glued bond (Samudrala, et al. 2002), or to frictional strength τ_f of the interface due to the remote compressive stress *P* (Xia et al., 2004, 2005; Lu et al., 2007). Because cracks have not been observed to form in this frictional configuration, we applied an adhesive bond to the interface, thereby strengthening the interface by the amount τ_0. The total interface strength is:

$$\tau_p = \tau_f + \tau_o. \quad (2)$$

Here, τ_o is a constant material property of the bond, $\tau_f = f\sigma_n$ where f is the friction coefficient, and σ_n is normal traction resolved on the interface. Because transient stress state $\Delta\sigma_{ij}$ is proportional to total interface strength τ_p, adding cohesive strength τ_o should magnify off-fault stress, encouraging tensile failure of the Homalite. In the configuration shown in Figure 1B, the greatest tensile stress (and thus tensile cracking) is expected in the lower block for a rupture propagating downward to the right.

PRODUCTS OF DYNAMIC SHEAR RUPTURE

Ruptures in these experiments propagated with velocities in the range $0.7c_s < v_{II} < 0.85c_s$, where in Homalite c_s = 1255 m/s (Fig. 4 and S1). Photoelastic images reveal tensile microcracks initiate within the region of stress concentration directly behind the dynamic shear rupture tip. Figure 2A shows fringe patterns at three times around a propagating rupture in an experiment with axial load *P* = 32 MPa and inclination angle α = 60°. A closer view of the shear rupture tip at 105 μs (Fig. 2B) reveals a trailing line of dark spots at an acute angle to the interface. These are shadow spots surrounded by caustics (Rosakis et al., 2000) associated with propagating tensile microcrack tips (Fig. 2C). The trailing edge of this triangular zone marks the point at which the microcracks stop growing: behind this zone static microcracks are left in the wake of the propagating rupture (Fig. 2B, C). This zone, between 5-10 mm in length (Fig. 2B,C), corresponds to the shear cohesive end zone of the propagating shear rupture. These observations confirm that the microcrack formation is a dynamic phenomenon triggered by the transient stress field of a propagating shear rupture and that the microcracks grow only in close proximity to the shear rupture tip.

Tensile microcracks (Fig. 3) were produced during shear rupture in all experiments at α = 60° and 70°, but microcracks were not observed at α = 80°. For greater values of α, remote compressive stress *P* resolves lesser normal and shear tractions on, and greater compression parallel to, the interface, which would inhibit tensile cracking. Consistent with theoretical calculations (Samudrala et al., 2002), all cracks formed in the tensile quadrant, nucleated on the

interface and grew into the Homalite (Fig. 3). In all cases, microcracks formed at high angles to the rupture interface and some curved slightly as they propagated into the Homalite sample (Fig. 3B). Longer microcracks typically are interspersed with shorter microcracks, and crack size and spacing is greater at $\alpha = 60°$ than $\alpha = 70°$. Maximum microcrack length changes systematically with distance from the nucleation site of the shear rupture, increasing from initial occurrence at ~3 cm to a maximum (up to ~5mm in length at $\alpha = 60°$) at ~ 9 cm, and then the length steadily decreases toward the edge of the sample (e.g., Fig. 3A). The increase in microcrack dimension with distance from the nucleation site is accompanied by an increase in stress concentration as evidenced by expansion of the lobes in the isochromatic fringe pattern focused around the rupture tip (Fig. 2A). Microcracks typically are shorter for greater rupture interface inclination angles α, reaching a maximum length of ~2.5 cm at $\alpha=70^o$. Longer microcracks extend across the entire thickness of the sample, while shorter microcracks do not (Fig. 3C). For $\alpha = 60^o$ the average width (measured across the out-of-plane dimension of the specimen) of microcracks is 0.35 ± 0.16cm whereas the average width for $\alpha = 70^o$ is 0.25 ± 0.19cm. Average microcrack spacing for $\alpha = 60^o$ is 0.35cm ± 0.29cm, whereas spacing for $\alpha=70^o$ is 0.23 cm ± 0.13cm. The larger microcrack width at smaller inclination angle is consistent with overall larger relative crack size as suggested by the length measurements. Average crack spacing appears to have a weak, inverse dependence on v_{II}, tending to be smaller at faster v_{II}.

Tensile microcracks grew in the velocity range $0.25c_s < v_I < 0.33c_s$ (Fig. S2). The microcracks were never observed to branch, which is consistent with propagation velocities on the order of $v_I \approx 0.3c_s$, less than the critical branching velocity (e.g., Fineberg et al., 1991; Sagy et al., 2001, 2002).

The inclination angle θ (Fig. 3C, Fig. S1), between the tensile microcrack and the interface for cracks longer than ~0.1 mm was measured on photomicrographs taken with an optical microscope focused at mid-thickness of the Homalite samples. Microcrack orientation, θ, varies within individual experiments by as much as ~15° (Fig. S1). By comparing θ and v_{II} variations from all experiments it is clear that θ correlates with v_{II}; however, v_{II} is not the only parameter influencing microcrack inclination.

To compare experiments we bin microcrack orientation data from velocity-distance plots (e.g. Fig. S1) with bin centers at locations where rupture velocities were calculated. We plot average crack angle θ over each bin against the corresponding rupture velocity for each experiment in Figure 4. This data comprises six experiments representing two different loading configurations ($\alpha = 70°$, $P = 38$ MPa; and $\alpha = 60°$, $P = 32$ MPa). Two distinct trends show inclination angle increasing almost linearly with rupture velocity. The offset between the two trends is a measure of the influence of σ_{ij}^0 on microcrack orientation, i.e., $\Delta\theta = 7–8°$ for $\Delta P = 6$ MPa and $\Delta\alpha = 10°$.

VELOCITY WEAKENING MODEL OF A SUB-RAYLEIGH SHEAR RUPTURE GROWING ALONG A WEAK INTERFACE

The purpose of this section is to determine the local nature of the dynamic stress field at the vicinity of the tip of the main shear rupture which is growing along a weak plane (fault) with sub-Rayleigh speed. It is this stress field which is responsible for driving the off-fault mode-I microcracks of interest for the present study.

As can be seen from the previous sections, measurable variations of shear rupture speed exist during each of the experiments. However, such variations are gradual and are typically less than 10% of the shear wave speed of the solid. This observation together with the experimental fact that the off-fault microcracks are generated dynamically at the immediate vicinity of the rupture tip allow us to use a dynamic, "steady-state" rupture model in the current section. Indeed, as shown by Freund and Rosakis (1992) for the mode-I case and by Liu and Rosakis (1994) for mixed-mode, the local near-tip field of a growing rupture always retains its steady-state structure at sufficiently close distances from the rupture front, even if substantial accelerations or decelerations are present.

The additional observation that the microcracks continue to grow for some short time after the rupture tip has passed by, further implies that a model featuring a "distributed" rather than a "point" rupture zone would be necessary to capture the physics of the problem. In particular, a sub-Rayleigh modification of the steady-state and velocity weakening shear cohesive zone model by Samudrala et al. (2002) is a viable candidate to adopt for the current study. Our preference in modeling the cohesive and frictional resistance of the interface (fault) by a velocity weakening rather than a slip weakening law (despite its relative complexity) is due to experimental evidence, recently reported by Lu et al. (2007) on the basis of similar rupture experiments in Homalite-100. In these experiments, the attainment of both "crack-like" and "pulse-like" shear ruptures in frictional interfaces separating identical Homalie-100 plates, provided strong evidence of the activation of a velocity weakening mechanism during rupture. As described by Zheng and Rice (1998), velocity weakening is the dominant mechanism promoting pulse-like shear ruptures at an interface separating identical solids.

On the basis of the above arguments, we consider a semi-infinite, planar shear rupture (mode-II rupture) propagating dynamically along a weak interface separating two identical, homogenous, isotropic, linear elastic solids. The rupture features a shear rupture end zone of length L, translating in the front of the rupture tip. The rupture tip propagates at a constant, sub-Rayleigh speed v_{II} ($0 \leq v_{II} \leq c_R$) in its own plane under either plane strain or plane stress conditions. In the particular problem, shown in Fig.5, plane stress is the appropriate approximation since the two plates separating the interface are "thin" compared to their in-plane dimensions.

An orthonormal coordinate system $(0; x_1, x_2, x_3)$ is placed with its origin at the rupture nucleation site and with the (x_1, x_2) plane containing the center plane of the specimen. The positive x_1 axis lies along the fault line in the direction of rupture growth. The x_2 axis is perpendicular to the fault and faces towards the upper part of the specimen, while the x_3 axis points out of the plane of Fig. 5 and is not shown. An additional moving coordinate system $(\eta_1, \eta_2) = (x_1 - v_{II}t, x_2)$ centered at the front end of the shear cohesive zone as shown in Fig. 6.

The constitutive description of shear traction in the cohesive zone τ is given by a linear velocity weakening law, which relates the cohesive shear traction at any point within the cohesive zone to the local slip velocity $\dot{\delta} \equiv (\dot{u}_1^+ - \dot{u}_1^-)$, as follows:

$$\tau(\dot{\delta}) = \tau_0 \left[1 + \beta^* \frac{\mu \dot{\delta}}{2\tau_0 c_s} \right]. \tag{3}$$

In the above expression μ is the surrounding material's shear modulus, τ_0 is the static shear cohesive strength of the interface while $\beta^* < 0$ is a negative dimensionless parameter (velocity weakening parameter) which governs the severity of velocity weakening and eventually needs to be determined by experiment. As described in previously, the static strength τ_0 is given by $\tau_0 = \tau_c + f_s P \cos^2 \alpha$. The total strength τ_0 is the net quasi-static strength level encountered by the shear rupture tip (front of the translating cohesive zone) as it races along the interface. Within the cohesive zone, this level drops to zero due to the linear velocity weakening law described in Eq. (3). It should be noted that although the dependence on τ on sliding speed, $\dot{\delta}$, is linear, the spatial distribution of $\tau(\eta_1/L)$ within the cohesive zone is not and needs to be determined by solving the complete boundary value problem as posed above.

We omit the derivations here for brevity, and simply include the results. The normalized dynamic shear stress σ_{12} distribution on the upper rupture face of the cohesive zone can be obtained as follows:

$$\frac{\sigma_{12}}{\tau_0} = \frac{\tau}{\tau_0} = 1 + \frac{\sin \gamma\pi}{\pi} \frac{(-\eta_1/L)^{\gamma+1/2}}{(1+\eta_1/L)^{\gamma}} \int_0^1 \frac{(1-s)^{\gamma}}{\sqrt{s}\,(1+s\,\eta_1/L)} ds\,, \tag{4}$$

where $\gamma = \frac{1}{\pi} \tan^{-1}\left[\beta^* \frac{v^3}{c_s^{\,3}} \frac{\alpha_s}{R(v_{II})}\right] < 0$, $R(v_{II}) = 4\alpha_l\alpha_s - (1+\alpha_s^2)^2$ is the Rayleigh function.

Figure 7 shows the distribution of dynamic shear stress σ_{12} on the upper (or lower) rupture face of the cohesive zone. The dynamic shear stress decreases monotonically from τ_0 at the mathematical rupture tip (leading edge of the cohesive zone) and approaches zero at the physical rupture tip (trailing end of the cohesive zone).

The distribution of the normalized dynamic stress component, σ_{11}, on the upper rupture face of the cohesive zone is given by:

$$\frac{\sigma_{11}}{\tau_0} = -\frac{4}{\pi} \frac{(\alpha_l^2 - \alpha_s^2)\alpha_s}{R(v_{II})} \frac{(-\eta_1/L)^{\gamma+1/2}}{(1+\eta_1/L)^{\gamma}} \cos \gamma\pi \int_0^1 \frac{(1-s)^{\gamma}}{\sqrt{s}\,(1+s\,\eta_1/L)} ds + \frac{T}{\tau_0}\,. \tag{5}$$

On the lower rupture face, however, the normalized dynamic stress component σ_{11} is different from Eq. (5) and features a change in sign only in its first term. The direct stress component, acting parallel to the fault line, now becomes:

$$\frac{\sigma_{11}}{\tau_0} = \frac{4}{\pi} \frac{(\alpha_l^2 - \alpha_s^2)\alpha_s}{R(v_{II})} \frac{(-\eta_1/L)^{\gamma+1/2}}{(1+\eta_1/L)^{\gamma}} \cos \gamma\pi \int_0^1 \frac{(1-s)^{\gamma}}{\sqrt{s}\,(1+s\,\eta_1/L)} ds + \frac{T}{\tau_0}\,. \tag{6}$$

It should be note that the direct stress T-term in the above equations does not change sign as one moves from the upper to the lower rupture faces. It represents a constant background pre-stress state which also trivially satisfies both the governing equations and the boundary conditions of the rupture problem as stated above. Its magnitude can be related to the applied pre-stress on the specimen boundaries and to the fault inclination angle.

Figure 8 (a) and 8(b) show the distribution of the dynamic stress, σ_{11}, on the upper and lower faces of the rupture plane respectively. The different curves correspond to various levels of rupture speed. Results are shown for $\beta^* = -0.4$, P = 32MPa and $\alpha = 60^0$.

PREDICTING THE ORIENTATION OF TENSILE CRACKS

Both Homalite-100, used in the experiments, and crustal rock surrounding natural faults in earthquake events are nominally brittle solids. Consequently we assume that they obey the maximum principal stress criterion for brittle fracture. Equivalently, we assume that the secondary, mode-I, cracks observed in the experiments and on exhumed faults would initiate on the side of the fault and at locations which, locally and instantaneously, experience sufficient tensile stresses as the dynamic shear rupture passes by. For right lateral slip, as in the present study, this is the lower face of the main shear rupture. In particular, these secondary (mode-I) cracks would initiate at positions just below the fault plane (weak bond) where the maximum stress equals the ultimate tensile strength of the monolithic material. Also, it is expected that their initial direction of growth will be coincidental to the principal stress direction at such locations. At points adjacent to the cohesive zone, the dynamic stress component σ_{11} is always negative (compression) on the upper surface. On the lower surface of the fault plane however, σ_{11} could attain positive (tensile) values near the physical crack tip as is clearly shown in Fig. 8(b). The exact location at which σ_{11} change sign depends on the relative magnitude of the negative T-term ($T = -P\sin^2\alpha$) compared to the positive, dynamic first term in Eq. (6).

As anticipated, the rupture speed, far-field tectonic load, *P*, the angle α, as well as the static strength and the velocity weakening parameter, all contribute to identifying the location along the bottom faces of the fault line where this stress component may first become positive. The relevant stress however which governs the initiation of tensile crack is the maximum principal stress, σ_1, rather than σ_{11} itself. A two dimensional Mohr's circle analysis may now be used to show that this stress on the upper surface of the shear cohesive zone is always less than that on the lower surface, and the latter may become large enough, close to the physical rupture tip, to reach the Homalite strength σ_H and thus initiate tensile fractures. To investigate such conditions, the stress state illustrated in Fig. 9, is used to calculate the maximum principal stress σ_1 and the inclination angle θ of the principal plane with the horizontal (fault plane) as follows:

$$\sigma_1 = \frac{\sigma_{11}}{2} + \sqrt{\left(\frac{\sigma_{11}}{2}\right)^2 + \sigma_{12}^2}\,, \tag{7}$$

$$\theta = \frac{\pi}{2} - \frac{1}{2}\arctan\left(\frac{2\sigma_{12}}{\sigma_{11}}\right). \tag{8}$$

Figure 10(a) and 10(b) show the variation of the normalized principal stress, σ_1/τ_0, and the principal angle respectively. These are plotted for points within the cohesive zone, $-L \le \eta_1 \le 0$, and on the lower rupture face. They correspond to *P* = 32MPa, α = 60^0, $v_{II}/c_s = 0.6$ and $\beta^* = -0.4$. They are obtained by substituting Eqs. (4) and (5) into Eqs. (7) and (8) respectively. As discussed above, the principal stress remains positive in a small region at the trailing end of the shear cohesive zone, allowing the maximum normal stress fracture criterion to be satisfied somewhere in that vicinity.

The approach shown in Figure 10 can be used to predict the initial inclination angle of the secondary microcracks for all loading configurations, (P,α), sub-Rayleigh shear rupture speeds, v_{II}/c_s and velocity weakening parameters, β^*. This is done by indicating the critical level for

fracture initiation $(\sigma_1 = \sigma_H)$ on the left vertical axis of Fig. 10. This allows for the identification of the location on the fault line (ordinate of Fig. 10) where the first secondary crack will initiate (see arrow from the left vertical axis of Fig. 10). By considering, the same location, the corresponding inclination angle, θ, can be obtained as indicated by the arrow for the right vertical axis in Fig. 10.

MICROCRACK INCLINATION ANGLE: THEORY VS. EXPERIMENT

We have seen that the laboratory experiments have revealed a strong correlation between θ and system parameters such as rupture speed, v_{II}, and tectonic loading (P, α). The model presented above also shows that in additional to the above, other parameters, such as the static bond strength, τ_0, the velocity weakening rate, β^*, and the tensile strength of monolithic Homalite, σ_H, are also involved in determining θ.

From the above parameters, some are easily measurable from independent experiments while other can only be estimated to vary within certain ranges. In particular the tensile strength of Homalite, σ_H, is reported to range from 18MPa to 28MPa. There is no experimental information regarding the amplitude of the negative velocity weakening parameter, β^*, for interfaces of the type considered in this study. As a result of these observations, the approach that was taken here was to treat these parameters as unknowns to be fitted by a single set of experimental conditions. When determined, these parameters were used in the theoretical model to predict the outcome of a series of subsequent experiments. The purpose of this exercise was to validate the model by checking its ability to determine the dependence of θ on v_{II}, α and *P*.

Experiment 60I ($P = 32\text{MPa}, \alpha = 60^0$) was randomly chosen to provide the best fit for σ_H and β^*. The discrete points in Fig. 11 represents the experimental dependence of θ on rupture speed v_{II}, while the solid line is the result of the theoretical model for $\sigma_H = 21\text{MPa}$ and $\beta^* = -0.61$. These values are chosen to provide the best fit to the experimental results of this particular experiment. The same data presented as the variations of θ along the rupture path (fault plane) are shown in Figure 12.

Using the above stated values for σ_H and β^* and the measured rupture speed history as input, the theoretical variation of θ along the rupture path can be computed for experiments number 70I and 70J ($P = 38\text{MPa}, \alpha = 70^0$) and these predictions can be compared to the actual measurements of θ. This comparison is shown Fig. 13(a) and 13(b).

It is observed that the model predictions (unlike Figs 11 and 12, Figure 13 does not represent fits) reproduce the measure values and the spatial variation of the secondary crack inclination angles well. It should be noted that although experiments 70I and 70J were nominally identical in loading configuration, they featured slightly different velocity histories due to uncontrollable differences in rupture nucleation conditions and load uniformity. Another way to view the same data is to concentrate on the dependence of θ on v_{II} for both 70I and 70J. The comparison between predictions and experiment for these cases are shown in Fig. 14(a), (b).

Close scrutiny of the above result reveals that for a given value of *P*, the dependence of θ on v_{II} is approximately linear. For fixed values of σ_H and β^*, the level and slope of this line depends on the value of the far-field stress *P* (see Figs. 11 and 14).

Finally it should be noted that a separate set of experiments was performed for $P = 56\text{MPa}, \alpha = 80^0$. The rupture speed ranged from 0.7 to 0.9c_s. For these conditions, no secondary cracks were observed. Indeed, application of the theoretical model for this case confirms that the brittle fracture initiation criterion is never satisfied within the cohesive zone. For this case, the large value of P ensures that the maximum principal stress remains below σ_H even at the trailing edge of the cohesive zone ($\eta_1/L \to -1$).

APPLICATION TO NATURAL FAULTS

The relative success of the simple analytical model developed here in predicting the presence of secondary, mode-I, cracks and their inclination angles relative to the main shear rupture, allows us to attempt its generalization and application to earthquake ruptures propagating along frictional faults separating crustal rocks. A slight modification is introduced to account for biaxial loading conditions in which the vertical load is still given by P while the horizontal load is given by bP ($0 \le b < 1$) as shown in Fig. 15. Under such circumstances, $T = -P\left(\sin^2\alpha + b\cos^2\alpha\right)$ while $\tau_0 = \tau_c + f_s P\left(\cos^2\alpha + b\sin^2\alpha\right)$. For purely frictional faults, $\tau_c = 0$, and f_s of crustal rock is close to 0.75. If the parameter b is in the range $1 + 2f_s^2 - 2f\sqrt{1+f_s^2} < b < 1$, the static friction can always hold the two sides of the fault interface together. If $0 < b < 1 + 2f_s^2 - 2f\sqrt{1+f_s^2}$, the ranges of inclination angle α which can be sustained by static friction are $0^0 < \alpha \le \tan^{-1}\left\{\frac{1}{2f_s b}\left[1 - b - \sqrt{(1-b)^2 - 4f_s^2 b}\right]\right\}$ and $\tan^{-1}\left\{\frac{1}{2f_s b}\left[1 - b + \sqrt{(1-b)^2 - 4f_s^2 b}\right]\right\} < \alpha \le 90^0$.

We start with the crack orientation dataset of Di Toro et al (2005a), and use various measurements of velocity weakening behavior of geomaterials at high sliding rates to estimate β^*. Initial results suggest that the theoretical analysis based on laboratory experiments can be successfully scaled to the natural case. These results also suggest that tighter constraints on velocity weakening constitutive behavior of rocks at high sliding rates and high normal stress will allow the physics of the shear rupture tip to be described with much greater certainty.

CONCLUSIONS

These experiments have yielded a series of important insights into tensile cracking around a propagating subsonic shear rupture subjected to compressive and shear pre-stress. Most importantly, we have established that the tensile microcracks are a dynamic phenomenon not confined to experiments performed under impact loading in the absence of static compressive stress. The opening micocracks formed systematically in the region of tensile stress concentration on one side of the propagating shear rupture, consistent with early experimental results (Rosakis et al., 2000), field interpretations (Di Toro et al., 2005a) and theoretical predictions (Samudrala et al., 2002; Di Toro et al., 2005a). This phenomenon was not observed in laboratory experiments using a similar configuration with identical materials, but in the

absence of interfacial cohesion (e.g., Lu et al., 2007). The necessity of cohesion speaks to the competing effect of frictional strength and fracture toughness in enabling or retarding formation of microcracks: fault damage in the form of tensile fracture should be more prevalent along "strong" faults (e.g. stress drop > 100 MPa, as defined by Kanamori (1994)), even in the presence of large compressive tectonic stress. Finally, the direction of tensile microcrack growth always makes an acute angle with the direction of shear rupture growth (Fig. 2).

Several other observations are thought provoking, and require further investigation. First, microcrack growth initiates on the interface near the shear rupture tip, and growth ceases when the rupture tip has moved ~5–10 mm beyond the microcrack. The orientation at which microcracks initiate is related to rupture velocity, v_{II}, and tectonic stress state (Fig. 4). We can quantify these effects using an analytical solution for a dynamic mode II crack following Samudrala et al. (2002). Using measurements of rupture velocity, crack angle, and static pre-stress state, we can inversely constrain these elusive parameters critical to defining the physics at the rupture tip.

This study suggests a fundamental connection between tensile, off-fault fractures and past earthquakes as the laboratory tensile microcracks are shown to be produced dynamically by transient stress perturbations due to a rapidly propagating shear rupture. Furthermore, we demonstrate that microcrack orientations correlate with rupture velocity and ambient stress.

METHODS SUMMARY

We conducted 28 experiments to investigate the phenomenon of secondary tensile microcrack formation by dynamic shear rupture along an interface (the model fault surface) with friction (due to the applied uniaxial load) *and* cohesion (due to the glued interface). Ruptures were induced along a precut interface in Homalite samples by exploding a nickel-cadmium wire embedded across the interface (Fig. 1A). Rupture interfaces were sawcut through initially intact square samples. Epoxy resin (Loctite 330 adhesive) was applied uniformly to one surface; Loctite 7387 activator was applied to the other surface; and the two surfaces were held together while curing to force excess resin out of the interface. The bond was cured for five hours at room temperature and the procedure produced a layer 20-50 μm in thickness between the two Homalite surfaces. To constrain the static coefficient of friction, f, and the cohesive shear strength, τ_o, of the bond we conducted static strength tests on 14 Homalite samples with glued interfaces at angles ranging from 30° to 80° using an Instron electromechanical testing machine. The samples were subjected to uniaxial loads (Fig. 1B) through a spherically seated platen moving at a steady downward displacement rate of 0.25 mm/s. The stress path during loading and stress drop at failure was recorded using a 100 kN load cell. The load at failure, P_{crit}, was used to calculate the resultant critical normal, σ_n, and shear tractions τ on the interface. The experimental strength envelope has a slope $f = 0.32 \pm 0.15$ and y-intercept $\tau_o = 11.3 \pm 1.5$ MPa, where the errors are one standard deviation of the residuals (Fig. 2C).

During the dynamic experiments, the samples were compressed under an axial stress P applied at an angle α to the normal to the interface (Fig. 1B). Test values of α were 60°, and 70° and 80°, and P varied between 30 and 38 MPa (corresponding to a range between ~85% and 98% of the limiting stress P_{crit}). Note that in these experimental configurations, the cohesive strength of the interface far exceeds the frictional strength. While this experimental ratio of cohesive to frictional strength may not represent the expected ratio for faults in the earth, the large cohesive strength is necessary in order to produce stress concentrations larger than the tensile strength of

the Homalite ($\sigma_T \approx 28$ MPa) which is much greater than typical tensile strength of rocks ($\sigma_T < 10$ MPa).

Using digital photographs of the photoelastic fringes, we were able to track the propagating rupture tip from the nucleation site (i.e. from the exploding wire) out to distances of 110mm. The distance to the rupture tip from the nucleation site was measured in sequential photographs. Velocities were then calculated at each measurement distance from a sixth order polynomial fit to the distance-time data.

Because the rupture velocity is less than the Rayleigh wave speed, elastodynamic waves travel away from the nucleation site faster than the speed of the rupture: near the edges of the sample interaction with reflected waves tend to slow the rupture down. In order to maximize the length of rupture free of such boundary effects, the nucleation site was shifted several centimeters upward to the left from the center of the sample (Fig. 1B). In most cases the velocity decreased as the rupture approached the edge of the sample (Fig. S1), and this is interpreted as a boundary effect due to reflected waves from the sample edges. Therefore we restricted our analyses to data from the first 100 mm of rupture growth.

REFERENCES CITED

Andrews, D. J., 2005, Rupture dynamics with energy loss outside the slip zone. Journal of Geophysical Research, 110, doi:1029/2004JB003191.

Chester, F.M., Evans, J.P., and Biegel, R.L., 1993, Internal structure and weakening mechanisms of the San Andreas fault: Journal of Geophysical Research, v. 98, p. 771–786, doi: 10.1029/92JB01866.

Cowan, D., 1999, Do faults preserve a record of seismic slip?-a field geologist's opinion: Journal of Structural Geology, v. 21, p. 2703–2719, doi: 10.1016/S0191-8141(99)00046-2.

Di Toro, G., Nielsen, S., and Pennachhioni, G., 2005a, Earthquake rupture dynamics frozen in exhumed ancient faults: Nature, v. 436, p. 1009–1012, doi: 10.1038/nature03910.

Di Toro, G., Pennacchioni, G., and Teza, G., 2005b, Can pseudotachylytes be used to infer earthquake source parameters? An example of limitations in the study of exhumed faults: Tectonophysics, v. 402, p. 3–20, doi: 10.1016/j.tecto.2004.10.014.

Fineberg, J., Gross, S.P., Marder, M., and Swinney, H.L., 1991, Instability in dynamic fracture: Physical Review Letters, v. 67, p. 457–460, doi: 10.1103/PhysRevLett.67.457.

Griffith, W.A., Di Toro, G., Pennacchioni, G., and Pollard, D.D., 2008, Thin pseudotachylytes in faults of the Mt. Abbot Quadrangle, Sierra Nevada California: Physical constraints on seismic slip: Journal of Structural Geology, v. 30, p. 1086–1094, doi: 10.1016/j.jsg.2008.05.003.

Kanamori, H., 1994, Mechanics of earthquakes, Annual Reviews of Earth and Planetary Science, v. 22, p. 207-237.

Kavaturu, M., Shukla, A., and Rosakis, A.J., 1998, Intersonic crack propagation along interfaces: experimental observations and analysis: Journal of Experimental Mechanics, v. 38, p. 218–225, doi: 10.1007/BF02325746.

Lu, X., Lapusta, N., and Rosakis, A.J., 2007, Pulse-like and crack-like ruptures in experiments mimicking crustal earthquakes: Proceedings of the Natlional Acadamy of Science, v. 104, p. 18931–18936, doi: 10.1073/pnas.0704268104.

Lykotrafitis, G., Rosakis, A.J., and Ravichandran, G., 2006, Self-Healing Pulse-Like Shear Ruptures in the Laboratory: Science, v. 313, p. 1765–1768, doi: 10.1126/science.1128359.
Mutlu, O., and Pollard, D.D., 2008, On the patterns of wing cracks along an outcrop scale flaw: a numerical modeling approach using complementarity: Journal of Geophysical Research, v. 113, doi: 10.1029/2007JB005284.
Poliakov, A.N.B., Dmowska, R., and Rice, J.R., 2002, Dynamic Shear rupture interactions with fault bends and off-axis secondary faulting: Journal of Geophysical Research, v. 107, doi: 10.1029/2001JB000572.
Rosakis, A.J., 2002, Intersonic shear cracks and fault ruptures: Advances in Physics, v. 51, p. 1189–1257, doi: 10.1080/00018730210122328.
Rosakis, A.J., Samudrala, S., and Coker, D., 2000, Intersonic shear crack growth along weak planes: Materials Research Innovation, v. 3, p. 236–243, doi: 10.1007/s100190050009.
Sagy, A., Reches, Z., and Roman, I., 2001, Dynamic fracturing: field and experimental observations: Journal of Structural Geology, v. 23, p. 1223–1239, doi: 10.1016/S0191-8141(00)00190-5.
Sagy, A., Reches, Z., and Fineberg, J., 2002, Dynamic fracture by large extraterrestrial impacts as the origin of shatter cones: Nature, v. 418, p. 310–313, doi: 10.1038/nature00903.
Samudrala, O., Huang, Y., and Rosakis, A.J., 2002, Subsonic and intersonic shear rupture of weak planes with a velocity weakening cohesive zone: Journal of Geophysical Research, v. 107, doi: 10.1029/2001JB000460.
Sharon, E., Gross, S. P., and Fineberg, J., 1996, Energy dissipation in dynamic fracture: Physical Review Letters, v. 76, p. 2117-2120.
Swanson, M.T., 1988, Pseudotachylyte-bearing strike-slip duplex structures in the Fort Foster Brittle Zone, S. Maine: Journal of Structural Geology, v. 10, p. 813–828, doi: 10.1016/0191-8141(88)90097-1.
Tsustumi, A. and T. Shimamoto, 1997, High-velocity frictional properties of gabbro, Geophysical Research Letters, v. *24*, pg. 699-702.
Wibberley, C.A.J., and Shimamoto, T., 2003, Internal structure and weakening effects of major strike-slip fault zones: the Median Tectonic Line in Mie Prefecture, Southwest Japan: Journal of Structural Geology, v. 25, p. 59–78, doi: 10.1016/S0191-8141(02)00014-7.
Willemse, E.J.M., and Pollard, D.D., 1998, On the orientation and patterns of wing cracks and solution surfaces at the tips of a sliding flaw or fault: Journal of Geophysical Research, v. 103, p. 2427–2438, doi: 10.1029/97JB01587.
Xia, K., Rosakis, A.J., and Kanamori, H., 2004, Laboratory earthquakes: The sub-Rayleigh-to-supershear rupture transition: Science, v. 303, p. 1859–1861, doi: 10.1126/science.1094022.
Xia, K., Rosakis, A.J., Kanamori, H., and Rice, J.R., 2005, Laboratory Earthquakes Along Inhomogeneous Faults: Directionality and Supershear: Science, v. 308, p. 681–684.
Yamashita, T., 2000, Generation of microcracks by dynamic shear rupture and its effects on rupture growth and elastic wave radiation: Geophysical Journal International, v. 143, p. 395–406, doi: 10.1046/j.1365-246X.2000.01238.x.
Yuan, F. and V. Prakash, 2008, Use of a modified torsional Kolsky bar to study frictional slip resistance in rock-analogue materials at coseismic slip rates, International Journal of Solids and Structures,v. 45, pg. 4247-4263.

FIGURES

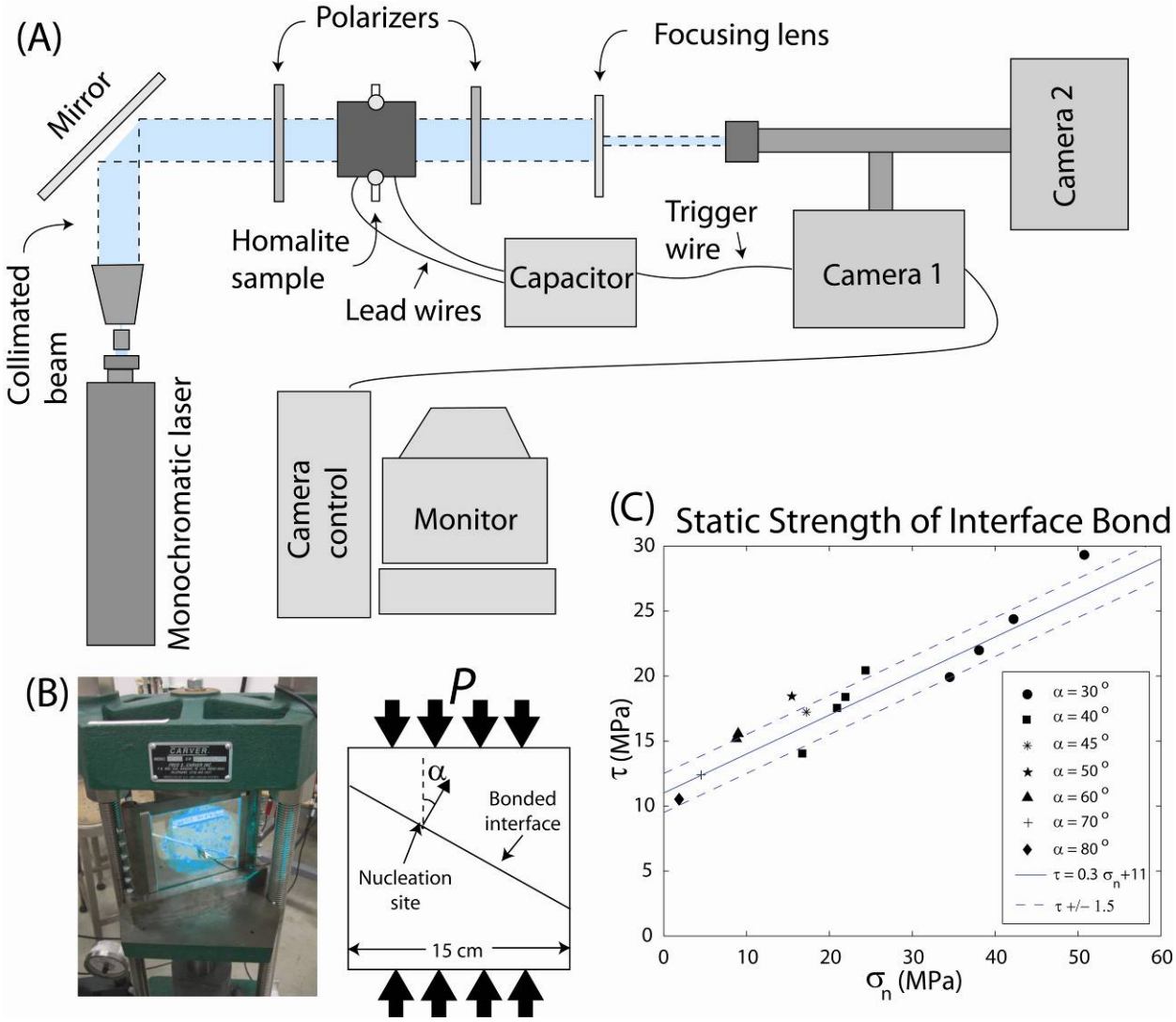

Figure 1. (A) Photoelastic apparatus including laser light source, polarizing filters, and high speed cameras. (B) Hydraulic press and sample configuration showing the relative orientation of the vertical load (*P*) and inclination of the interface (α).Explosion induces a bilateral right-lateral shear rupture. (C) To constrain the parameters f_s (coefficient of static friction) and τ_o we conducted static strength tests on 14 Homalite samples with glued interfaces at angles ranging from 30° to 80° using an Instron electromechanical testing machine. The samples were subjected to uniaxial loads in the configuration shown in (B). The experimental failure loads define a strength envelope with slope f_s = 0.32 ± 0.15 and Y-intercept τ_o = 11.3 ± 1.5 MPa, where the errors are plus or minus one standard deviation of the residuals. See Supplementary Material for further detail.

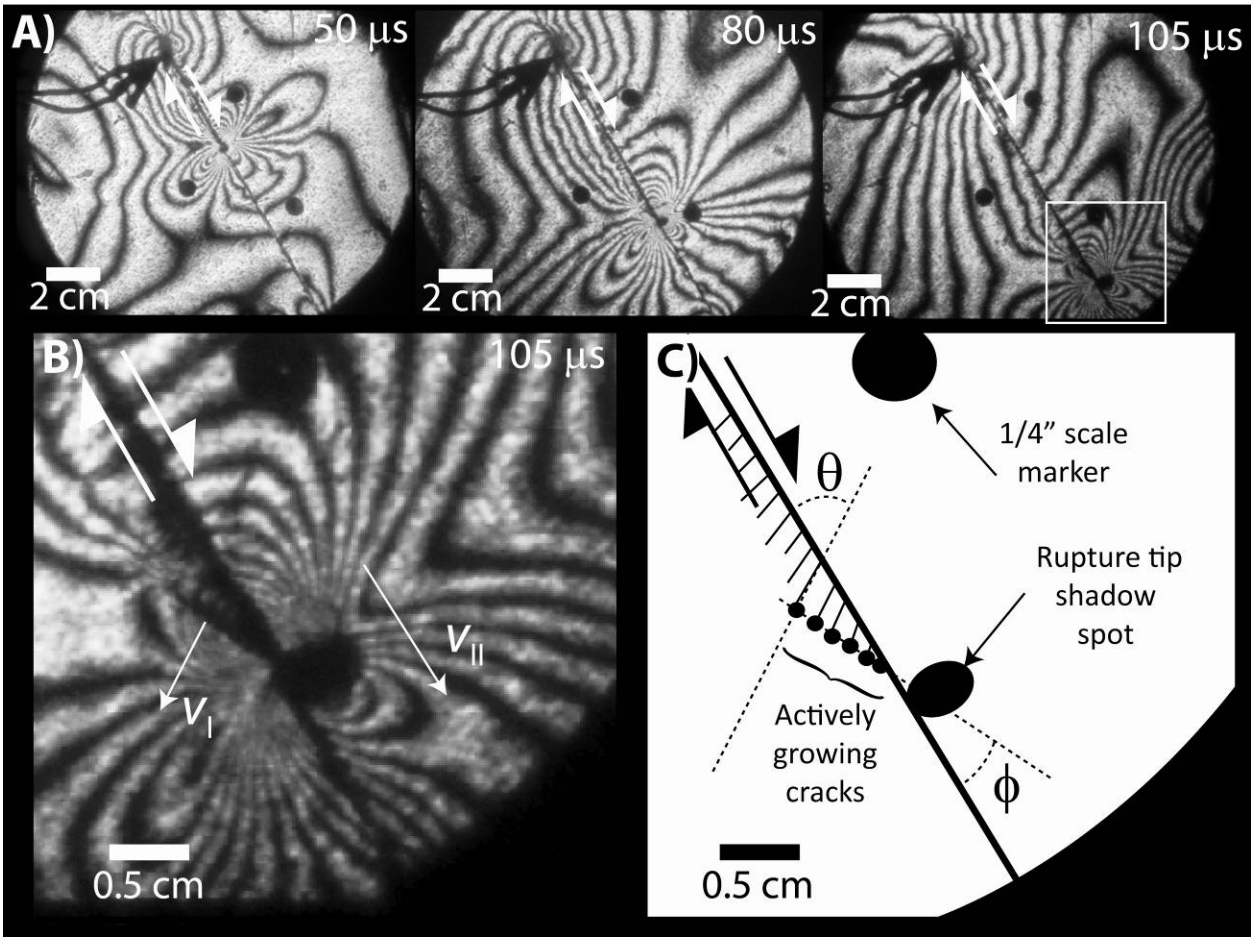

Figure 2. Isochromatic fringe patterns around a shear rupture nucleating at an exploding wire and propagating along the bonded interface. Note that the fringes surrounding the rupture tip expand as the rupture grows, indicating an increasing stress concentration with distance. (A) Photographs at 50, 80, and 105 μs after detonation. White box in the last photo indicates location of image in (B). (B) Close-up of rupture tip showing caustics associated with tensile microcrack tips. (C) Schematic of (B), identifying shadow spots, tensile microcracks, and defining angles θ and φ. All images are from experiment 60I, with *P* = 32 MPa and α = 60°.

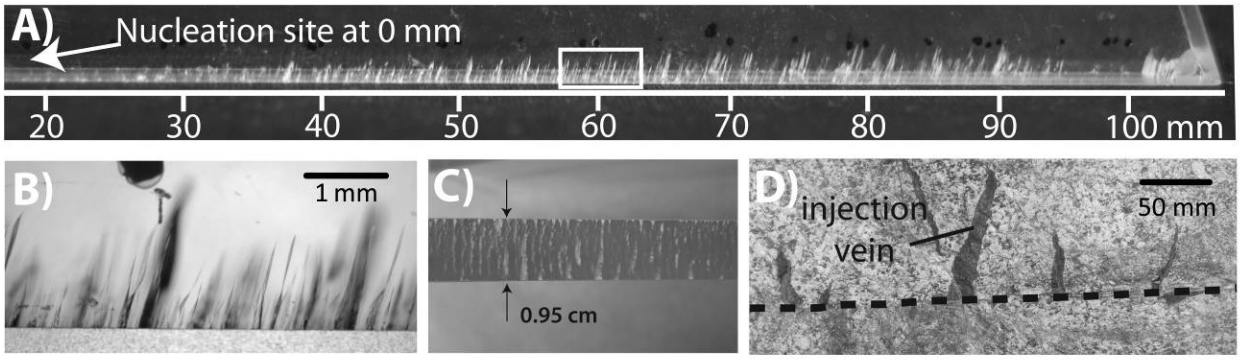

Figure 3. Tensile microcracks in Homalite 100 specimen 70I, *P* = 38MPa and α = 60°. (A) View of the 10 cm long array of microcracks along the rupture interface. White box shows location of image in (B). (B) Transmitted light microscopic image of microcracks. (C) View of the rupture interface surface. Larger microcracks frequently extend across the sample thickness, while smaller microcracks only partially cut

sample. Samples are ~0.95 cm in thickness. (D) Photograph of pseudotachylyte injection veins along a fault in the Adamello Batholith.

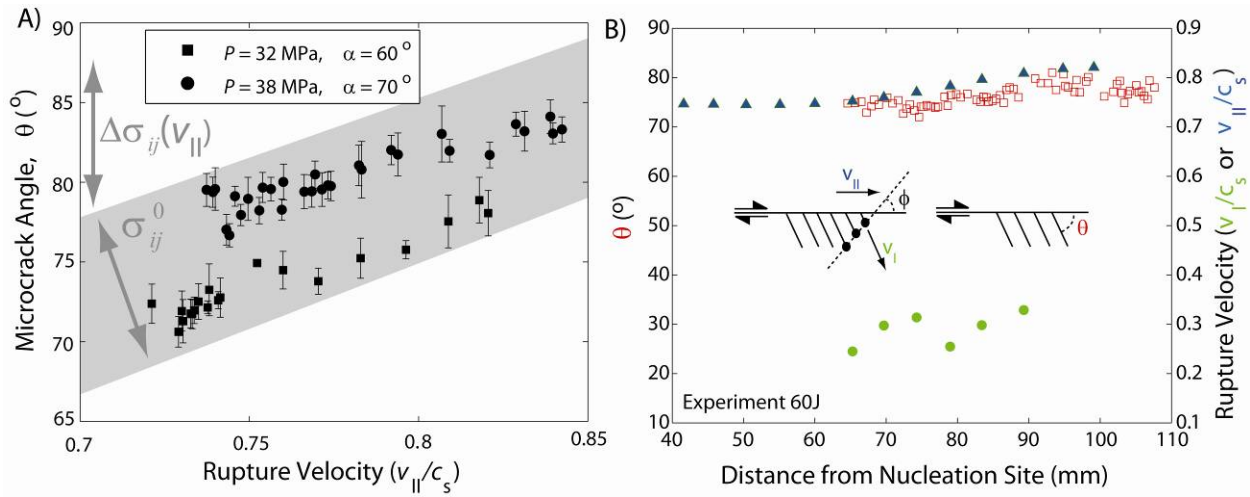

Figure 4. (A) Summary plot of average θ versus shear rupture velocities for six experiments. Inclination of data trends represents the dependence of microcrack orientation on the transient stress, $\Delta\sigma_{ij}$, which is dependent on the rupture velocity, v_{II}. The offset between the two trends is a function of the background, prestress state, σ_{ij}^{0}. The error bars represent +/– one standard deviation for each of the intervals plotted. (B) Example of rupture velocity and crack angle data from experiment 60J. Empty squares are microcrack inclination angle (θ) measurements, filled triangles are average v_{II}, and filled circles are average v_I.

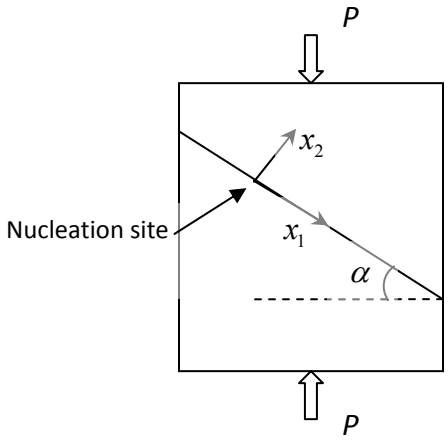

Figure 5. In-plane cross-section of specimen and fixed coordinate system (x_1, x_2). Origin at the nucleation site and positive x_1 axis along the rupture line.

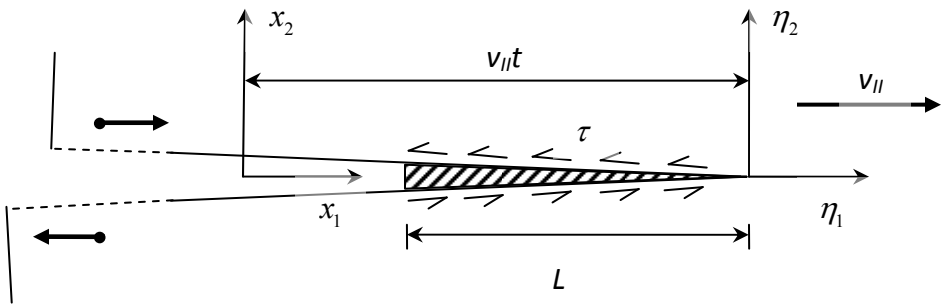

Figure 6. Moving and fixed coordinate systems of the rupture tip and the shear cohesive zone.

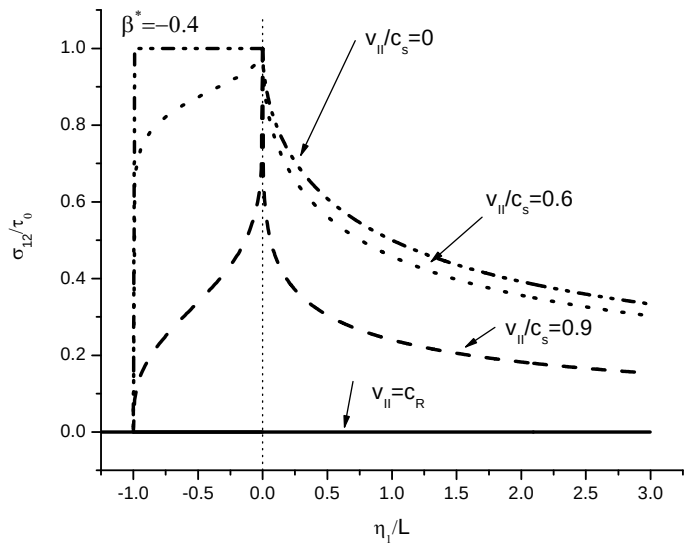

Figure 7. Distributions of ormalized of shear stress, σ_{12} , on the upper (or lower) rupture face.

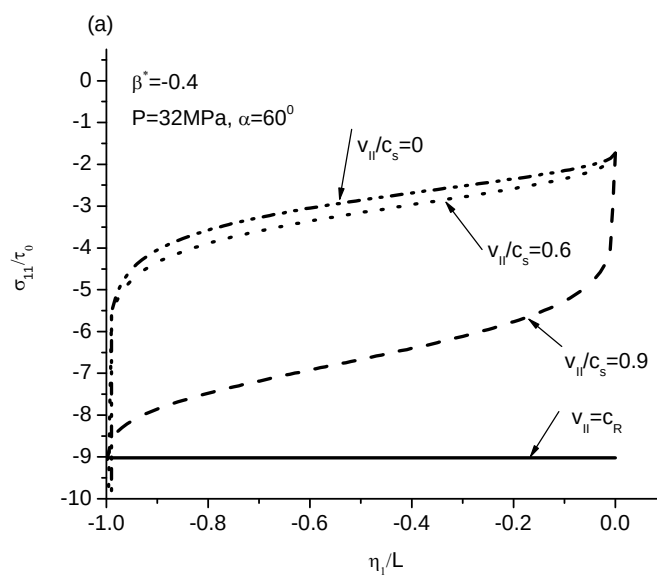

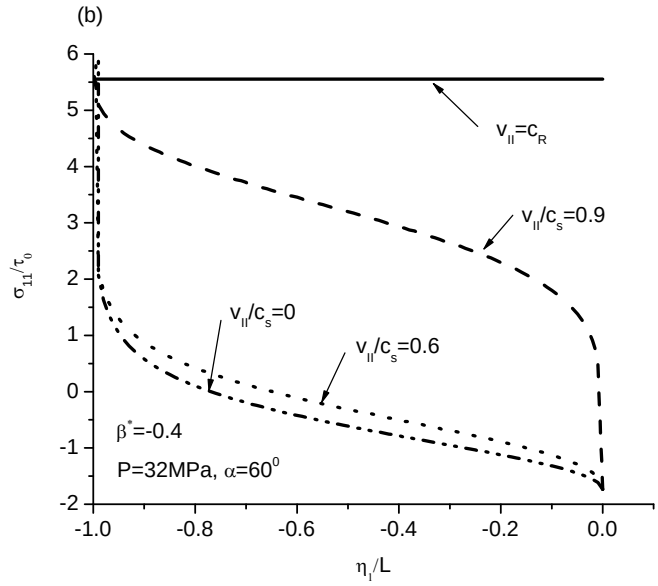

Figure 8. Distributions of normalized normal stress, σ_{11}, on a) upper rupture face, b) lower rupture within the cohesive zone.

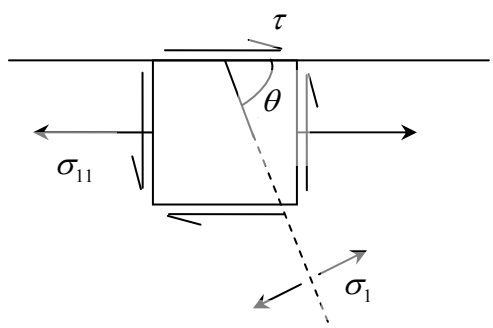

Figure 9. Stress state on the lower rupture surface.

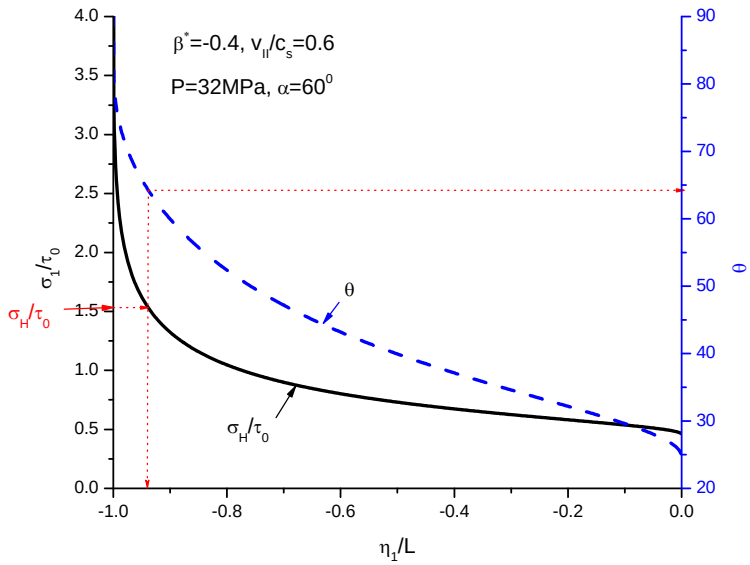

Figure 10. Method to determine the mode-I crack inclination angle.

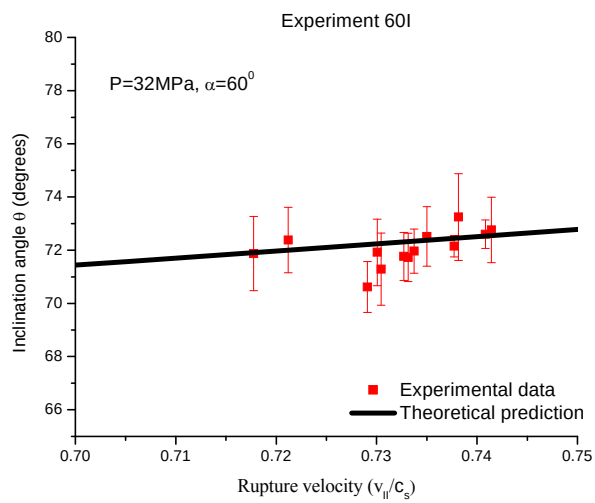

Figure 11. Theoretical and experimental inclination angle, θ, with respect to crack speed for experiment 60I. This experiment provides best-fit values for σ_H and β^*.

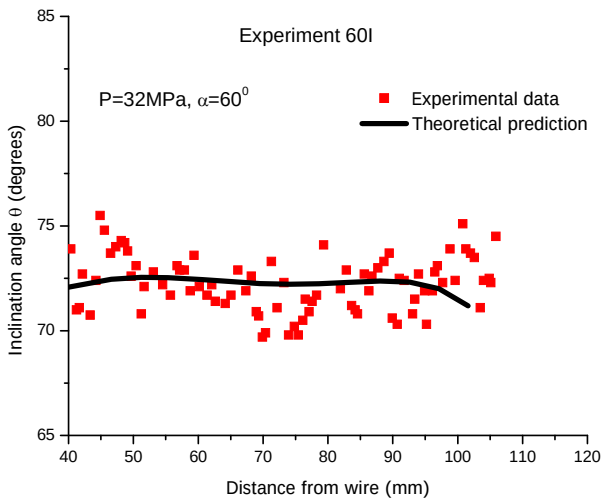

Figure 12. Theoretical and experimental inclination angle, θ, with respect to rupture distance from wire in experiment 60I.

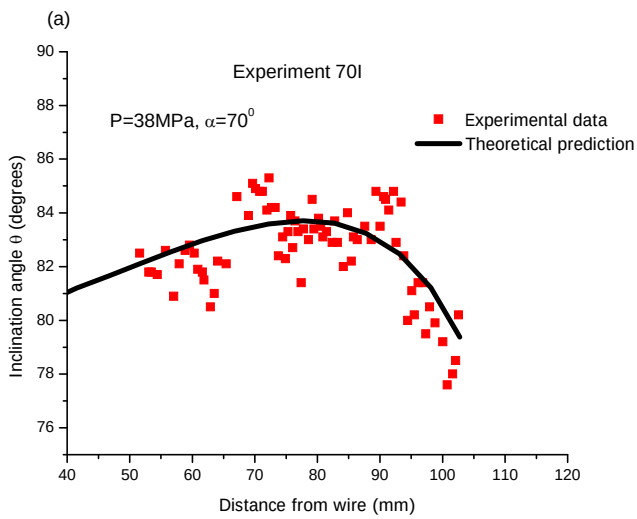

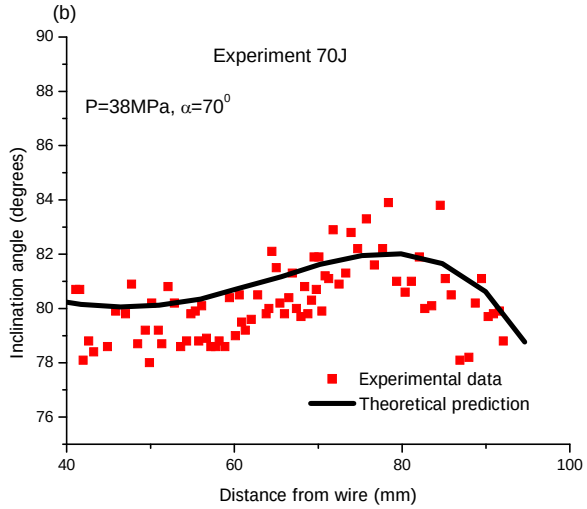

Fig. 13. Model predictions and experimental measurements of inclination angle, θ, with respect to rupture distance from wire in experiment a) 70I and b) 70J.

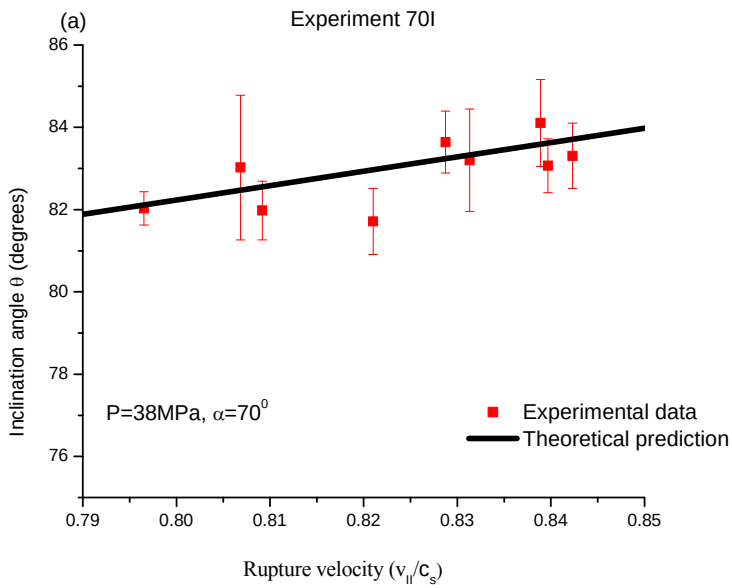

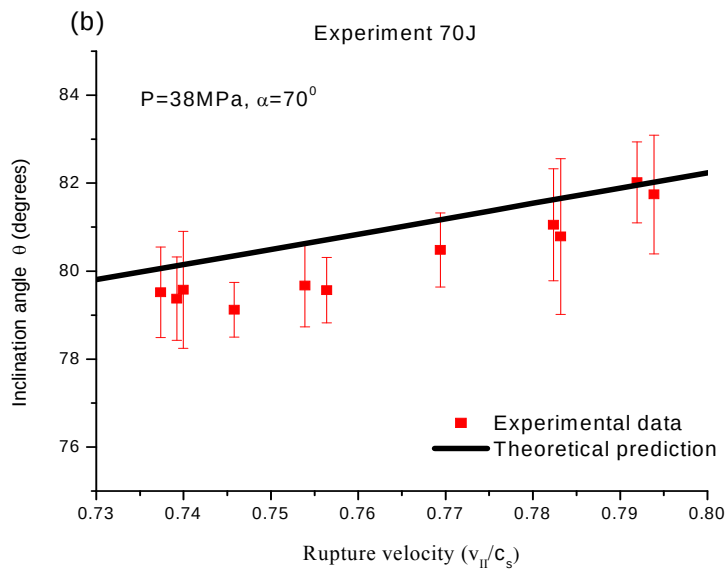

Fig. 14. Predicted and experimental inclination angle, θ, as a function of shear rupture speed a) Experiment 70I, b) Experiment 70J.

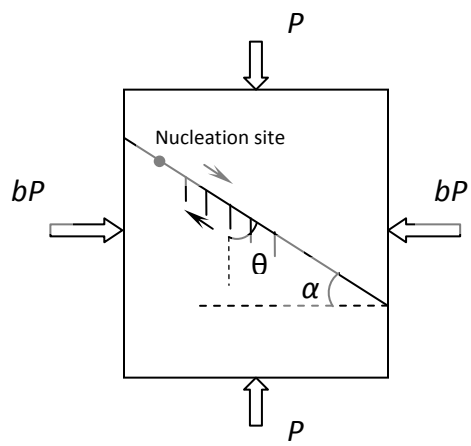

Figure. 15. Bi-axial loading configuration.

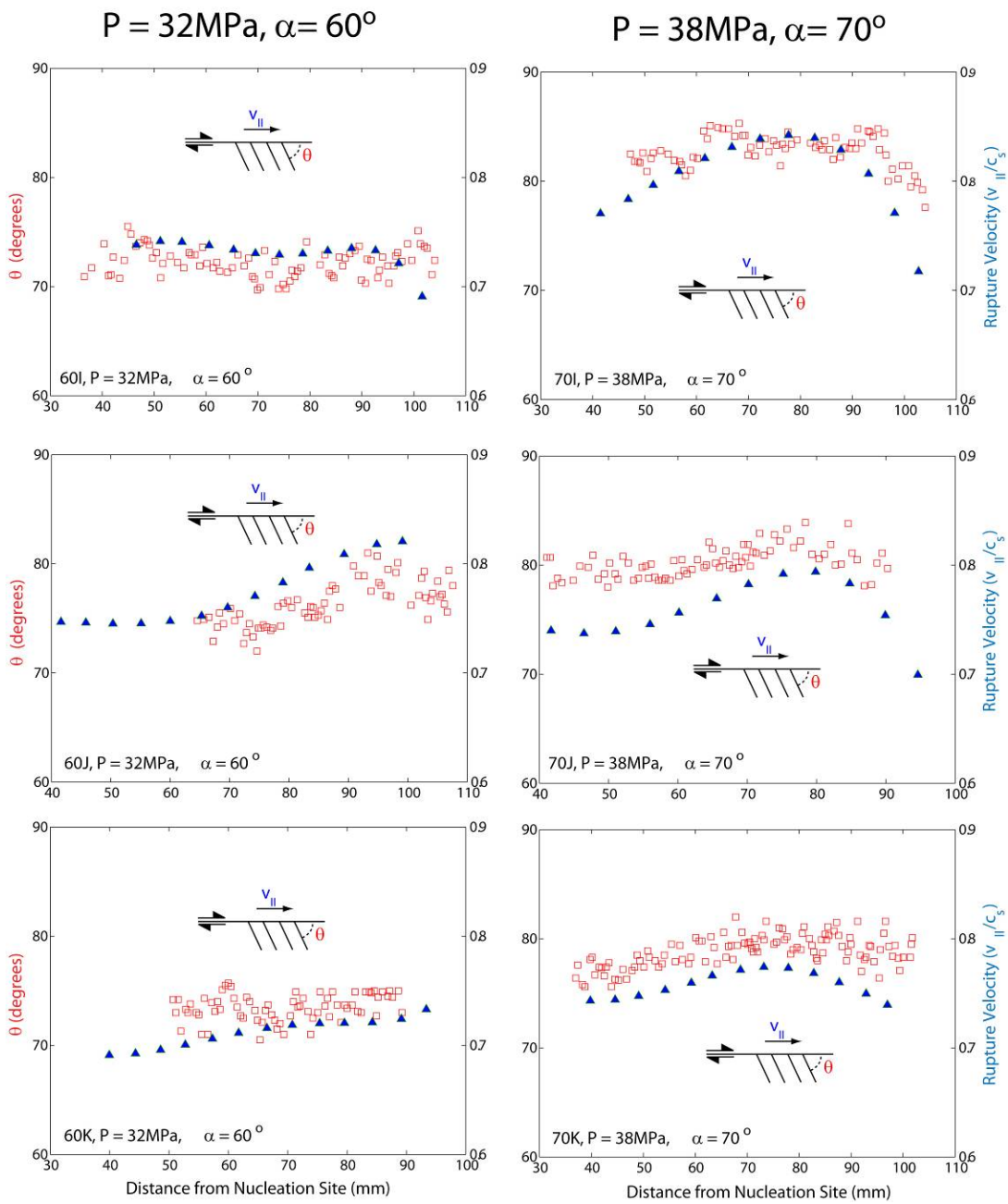

Figure S1: Shear rupture velocity, v_{II}, and microcrack angle, θ, versus distance of rupture tip from the nucleation site for experiments with (left column) P = 32 MPa and α = 60° and (right column) with P = 38 MPa and α = 70°.

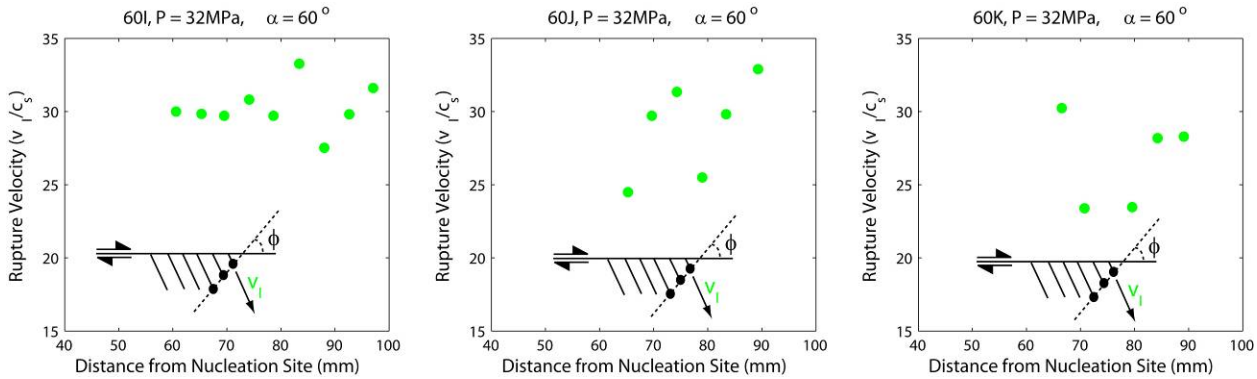

Figure S2: Opening microcrack rupture velocity, v_I, versus distance of the *shear* rupture tip from the nucleation site for experiments with P = 32 MPa and α = 60°

BIBLIOGRAPHY OF PUBLICATIONS SUPPORTED BY THIS GRANT

Griffith, W.A., A.J. Rosakis, D.D. Pollard, and C.-W. Ko, **2009**, Dynamic Rupture Experiments Elucidate the Source Mechanics of Ancient Earthquakes, *Geology*, **in press**

Griffith, W.A., A.J. Rosakis, D.D. Pollard, and C.-W. Ko, **2008**. Tensile cracks: a new link between geological observations of faults and seismological models of earthquake dynamics, American Geophysical Union, Fall Meeting, T22A-05.

Ngo, D., Y. Huang, A. J. Rosakis, W.A. Griffith, and D.D. Pollard, Inclination angles of secondary cracks in subsonic shear rupture with a velocity weakening cohesive zone, **in preparation**

COLLABORATORS INVOLVED IN THIS STUDY

- David D. Pollard, Department of Geologica and Environmental Sciences, Stanford University, Stanford, CA 94305, USA

- W. Ashley Griffith, Istituto Nazionale di Geofisica e Vulcanalogia, Rome, Italy (formerly PhD student with PI at Stanford)

- Ares J. Rosakis, Graduate Aeronautical Laboratory, California Institute of Technology, Pasadena, California, USA

- Chi-Wan Ko, Graduate Aeronautical Laboratory, California Institute of Technology, Pasadena, California, USA

- Youngang Huang, Department of Mechanical Engineering, Northwestern University, Evanston, Illinois, USA

- Duc Ngo, Department of Mechanical and Industrial Engineering, University of Illinois, Urbana, Illinois, USA